Strong Visible Light Absorption and Abundant Hotspots in Au-Decorated WO₃ Nanobricks for Efficient SERS and Photocatalysis

Jing-Wen Zou,[§] Zhi-Di Li,[§] Hao-Sen Kang,[§] Wen-Qin Zhao, Jing-Chuang Liu, You-Long Chen, Liang Ma,* Hua-Yi Hou,* and Si-Jing Ding*

Cite This: *ACS Omega* 2021, 6, 28347−28355

Read Online

ACCESS | Metrics & More | Article Recommendations | Supporting Information

ABSTRACT: Metal/semiconductor hybrids show potential application in fields of surface-enhanced Raman spectroscopy (SERS) and photocatalysis due to their excellent light absorption, electric field, and charge-transfer properties. Herein, a WO₃-Au metal/semiconductor hybrid, which was a WO₃ nanobrick decorated with Au nanoparticles, was prepared via a facile hydrothermal method. The WO₃-Au hybrids show excellent visible light absorption, strong plasmon coupling, high-performance SERS, and good photocatalytic activity. In particular, on sensing rhodamine B (RhB) under 532 nm excitation, bare WO₃ nanobricks have a Raman enhancement factor of 2.0×10^6 and a limit of detection of 10^{-8} M due to the charger-transfer property and abundant oxygen vacancies. WO₃-Au metal/semiconductor hybrids display a largely improved Raman enhancement factor compared to pure Au and WO₃ components owing to the synergistic effect of electromagnetic enhancement and charge transfer. The Raman enhancement factor and limit of detection are further improved, reaching 5.3×10^8 and 10^{-12} M, respectively, on increasing the content of Au to 2.1 wt %, owing to the strong plasmon coupling between the Au nanoparticles. Additionally, the WO₃-Au hybrids also exhibit excellent photocatalytic activity toward degradation of RhB under visible light irradiation. WO₃-Au (2.1 wt %) possesses the fastest photocatalytic rate, which is 6.1 and 2.0 times that of pure WO₃ nanobricks and commercial P25, respectively. The enhanced photocatalytic activity is attributed to the strong plasmon coupling and the efficient charge transfer between Au and WO₃ nanobricks. The as-prepared materials show great potential in detecting and degrading pollutants in environmental treatment.
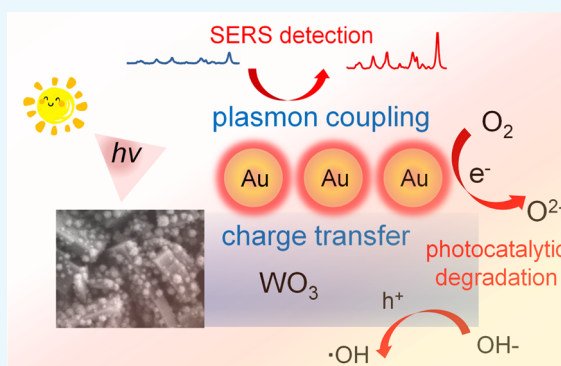
1. INTRODUCTION

Nowadays, the problem of pollution is becoming more and more serious along with the rapid development of industries. Many kinds of pollutants are being generated, such as atmospheric pollutants, water pollutants, and soil pollutants, which can mix with drinking water and food and harm the environment, greatly threatening the health of living things and human beings' survival. Thus, effective treatment of pollutants is particularly important. As advanced technologies, surface-enhanced Raman spectroscopy (SERS) and photocatalysis show great potentials in detecting and degrading pollutants and have been widely used in environmental treatment since their discovery.[1−5] In these two methods, Raman substrate materials and photocatalysts are essential prerequisites to achieve high-performance SERS and photocatalysis, respectively. Hence, the development of high-efficiency Raman substrates and photocatalysts becomes the most important issue.

In SERS measurements, the Raman signals of molecules and pollutants can be greatly amplified at a very low concentration in the presence of suitable substrate materials. Two well-known mechanisms for SERS are proposed, namely, electromagnetic

mechanism and chemical mechanism.[6−9] The electromagnetic mechanism is mainly based on the enhancement of the local electric field originating from plasmon excitation. Generally, plasmonic metals (such as Au, Ag, Cu) are the commonly used substrate materials to achieve high-performance SERS due to their tunable and large electromagnetic field.[10−15] However, the high cost and low stability and biocompatibility of plasmonic metals limit their utilization in practical applications. The chemical mechanism is mostly supposed to be caused by the charge transfer between the molecule and the substrate. Semiconductor materials with excellent optical and electrical properties are regarded as Raman substrates enabling the charge-transfer mechanism. Various semiconductor materials, such as TiO₂, WO₃, and MoS₂, have been developed for SERS-based applications due to their low cost and excellent stability
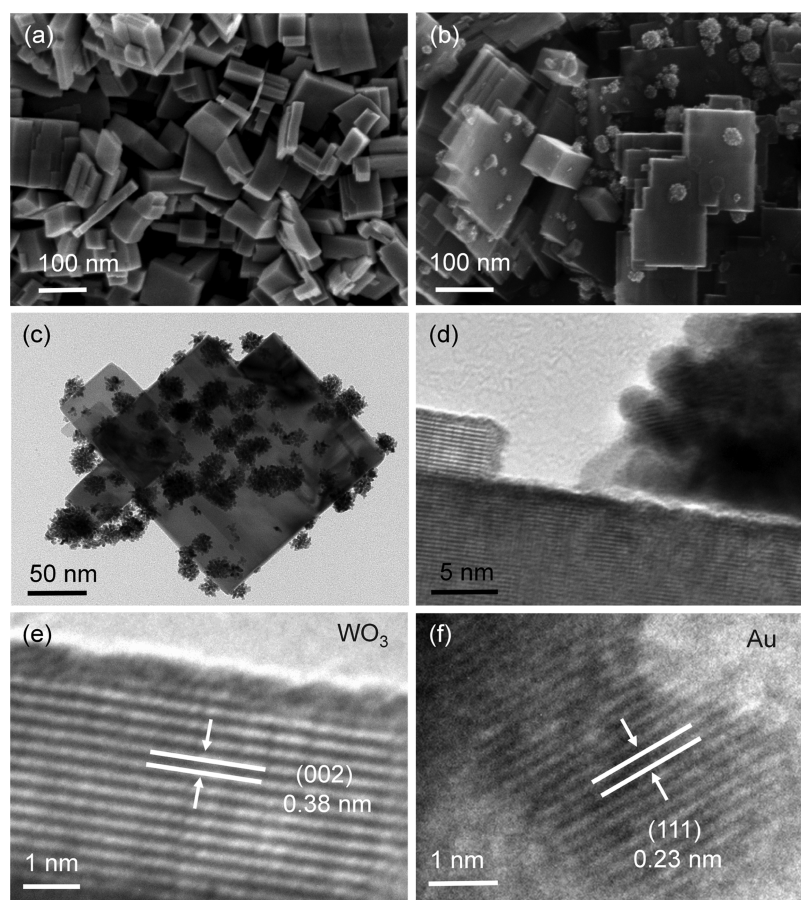
Figure 1. Morphology characterizations of WO_3 and WO_3-Au hybrids. SEM images of WO_3 nanobricks (a) and WO_3-Au (b). TEM (c) and HRTEM (d) images of WO_3-Au hybrids. Magnified HRTEM images of WO_3 (e) and Au (f).

and biocompatibility.[16−22] However, the Raman enhancement factor and the limit of detection of semiconductor-based substrates are too low compared with those of plasmonic metals.

Semiconductor-based photocatalysis is a green technology that is widely applied in solar-light-driven pollutant treatment.[23−25] In the past few years, large numbers of semiconductor materials have been used for photocatalytic decomposition of organic pollutants, while the real catalytic efficiency is quite low due to their poor visible light absorption and fast charge recombination rate. Besides being efficient SERS substrates, plasmonic metal nanocrystals with outstanding light absorption and strong electric field are also regarded as ideal antennas to achieve efficient photocatalysis.[26−30] The incorporation of semiconductor with plasmonic metal nanocrystal can dramatically enhance photocatalytic activity, owing to the improved light absorption, accelerated charge separation, and efficient plasmon energy transfer. Likewise, metal/semiconductor hybrids have also been proven to generate giant SERS signals due to the synergistic effect of electromagnetic enhancement and charge transfer.[31−36] There are several advantages when metal/semiconductor hybrids are used as SERS substrates. The charge-transfer efficiency is promoted due to the electron transfer between the plasmonic metal and the semiconductor. Meanwhile, the Raman enhancement factor is highly enhanced compared to the metal and semiconductor components, and it can be further enhanced by size control and morphological manipulation.[37−40] Therefore, it is worth constructing metal/semiconductor hybrids with high SERS sensitivity and photocatalytic activity that can efficiently detect and degrade pollutants.

In the present work, WO_3-Au metal/semiconductor hybrids were prepared and used as SERS substrates and photocatalysts, aiming to efficiently detect and degrade organic pollutants. Uniform WO_3 nanobricks and Au-decorated WO_3 hybrids were prepared through simple hydrothermal methods. The WO_3 nanobricks show excellent SERS sensitivity on detecting rhodamine B (RhB) under a 532 nm laser excitation. The Raman enhancement factor of the WO_3 semiconductor reaches 2.0×10^6 and the limit of detection reaches 10^{-8} M due to the charge-transfer property and abundant oxygen vacancies. Moreover, the SERS properties of the WO_3-Au hybrids with different contents of Au were investigated. The Raman enhancement factor is largely improved owing to the synergistic effect of electromagnetic enhancement and charge transfer. The Raman enhancement factor and the limit of detection are further improved, reaching 5.3×10^8 and 10^{-12} M, respectively, on increasing the content of Au to 2.1 wt %, owing to the strong plasmon coupling between the adjacent Au nanoparticles. Additionally, the WO_3-Au hybrids also exhibit excellent photocatalytic activity toward degradation of RhB under visible light irradiation. WO_3-Au (2.1 wt %) possesses the fastest photocatalytic rate, which is 6.1 and 2.0 times that of pure WO_3 nanobricks and commercial P25, respectively. Finally, the possible physical mechanism behind the enhanced photocatalysis is proposed based on the simulation and experimental results.
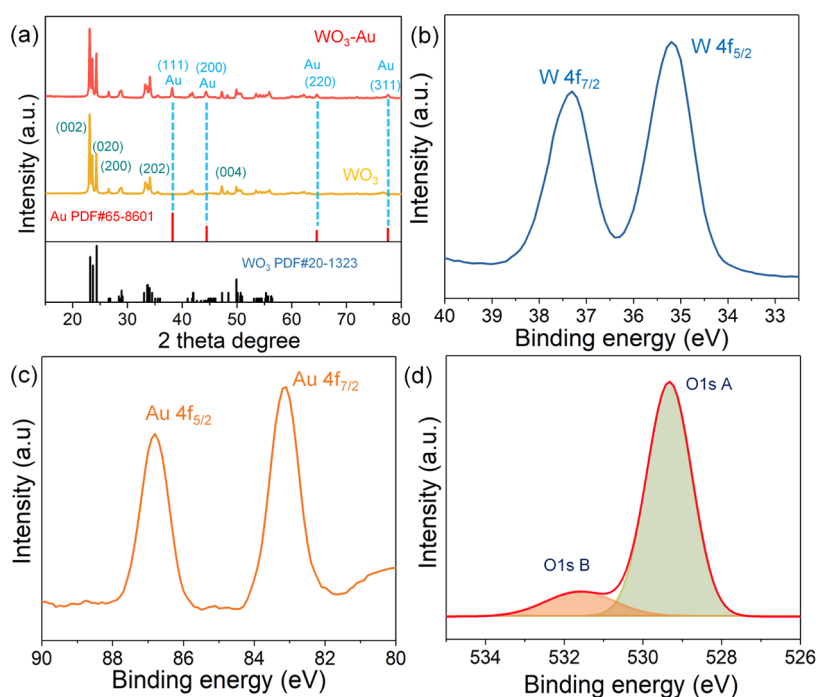
Figure 2. Component characterizations of WO_3-Au hybrids. (a) XRD patterns of WO_3 nanobricks and WO_3-Au hybrids. High-resolution XPS spectra of W 4f (b), Au 4f (c), and O 1s (d).
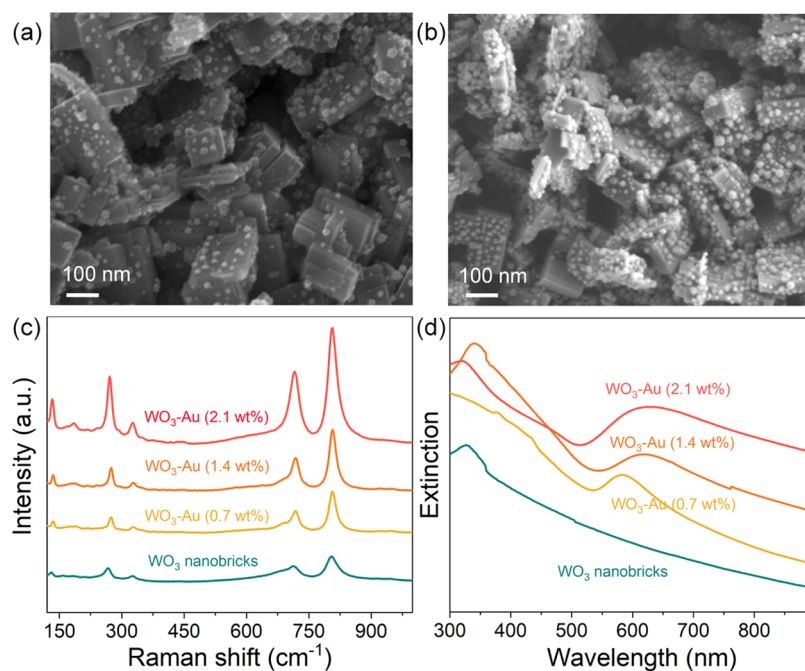

Figure 3. SEM images of WO_3-Au hybrids with 1.4 wt % (a) and 2.1 wt % (b) Au. Raman (c) and extinction spectra (d) of WO_3 and WO_3-Au with different contents of Au.

2. RESULTS AND DISCUSSION

WO_3 nanobricks were prepared by a one-step hydrothermal method, in which sodium tungstate was used as a precursor. The morphological characterization of WO_3 nanobricks was performed using scanning electron microscopy (SEM). Figures 1a and S1 show the SEM images of WO_3, indicating that WO_3 displays a uniform brick morphology and a smooth surface. Au-decorated WO_3 nanobricks were synthesized by growing Au nanoparticles on the WO_3 nanobricks, and chloroauric acid

and ascorbic acid were used as the precursor and the reductant, respectively. In Figure 1b, the SEM image of the Au-decorated WO_3 nanobricks is shown. The Au nanoparticles were randomly deposited on WO_3, and the brick morphology of WO_3 was well-maintained. The content of Au is determined to be about 0.7 wt % by inductively coupled plasma optical emission spectroscopy (ICP-OES) analysis. Transmission electron microscopy (TEM) was performed to further study morphology and the component of the WO_3-Au hybrids, and the results are shown in Figure 1c−f. The black spots with high
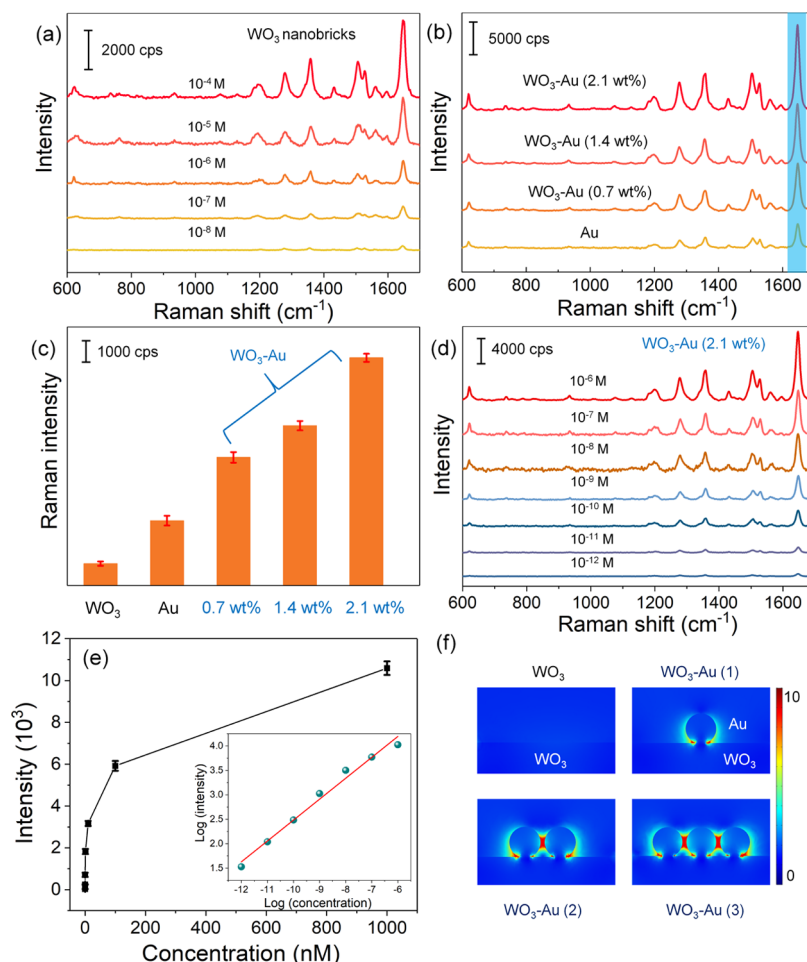
Figure 4. SERS activities of WO$_3$ and WO$_3$-Au hybrids. (a) Raman spectra of RhB with different concentrations of the substrates deposited on WO$_3$ nanobricks. (b) Raman spectra of RhB (10^{-6} M) absorbed on WO$_3$ and WO$_3$-Au hybrids with different contents of Au. (c) SERS intensity at the characteristic peak of 1647 cm^{-1} in the presence of WO$_3$ and WO$_3$-Au hybrids with different contents of Au. (d) Concentration-dependent SERS spectra for detection of RhB absorbed on WO$_3$-Au (2.1 wt %). (e) Plot of the peak intensity at 1647 cm^{-1} as a function of concentration; the inset represents the linear relationship. (f) Calculated electric field distributions of WO$_3$ and WO$_3$-Au hybrids deposited with one, two, and three Au nanoparticles.

contrast on the low-contrast WO$_3$ surface correspond to Au nanoparticles (see Figure 1c). The Au nanoparticles show a uniform flowerlike morphology and have an average size of 34 nm. High-resolution TEM (HRTEM) analysis is performed to detect the crystalline structure of the WO$_3$-Au hybrids. In Figure 1d, the HRTEM image of a Au-decorated WO$_3$ nanobrick is shown. Two different crystal lattices are clearly observed, indicating the possible presence of Au and WO$_3$. Figure 1e,f displays further magnified HRTEM images of WO$_3$ and Au. The WO$_3$ nanobrick shows continuous and ordered lattice fringes with a lattice spacing of 0.38 nm (see Figure 1e), corresponding to the (002) plane of triclinic WO$_3$. The spacing of the lattice fringe is 0.23 nm (see Figure 1f), which can be indexed to the (111) plane of Au. Figure S2 shows the energy-dispersive spectroscopy (EDS) spectrum of the WO$_3$-Au hybrids, and the presence of Au, W, and O can be observed.

Figure 2b shows the X-ray diffraction (XRD) patterns of WO$_3$ and WO$_3$-Au hybrids. The WO$_3$ pattern matches well with the triclinic-phase WO$_3$ (PDF # 20-1323). The peaks located at 23.1, 23.6, 24.1, 32.9, and 47.2° are ascribed to the (002), (020), (200), (202), and (004) planes of triclinic WO$_3$ (PDF # 20-1324), respectively. For WO$_3$-Au hybrids, the diffraction peaks located at 38.2, 44.6, 62.3, and 76.7° are

indexed to the (111), (200), (220), and (311) planes of Au (PDF # 65-8601), respectively. Meanwhile, the diffraction peaks of the triclinic-phase WO$_3$ are still observed, indicating the successful formation of hybrids. No characteristic peaks of any impurities are detected, suggesting high crystalline purity. X-ray photoelectron spectroscopy (XPS) analysis is further carried out to study the chemical state and the composition of WO$_3$-Au hybrids. The XPS survey spectrum clearly suggests that the sample mainly consists of Au, W, and O (see Figure S3). The high-resolution XPS spectra of O 1s, Au 4f, and W 4f peaks are shown in Figure 2b,c. In Figure 2b, the W 4f core level peak shown splits into two peaks at 37.3 (W 4f$_{7/2}$) and 35.2 eV (W 4f$_{5/2}$), indicating the existence of W^{6+}. Figure 2c shows the peaks of Au 4f$_{5/2}$ (86.8 eV) and Au 4f$_{7/2}$ (83.1 eV), proving the existence of Au in the hybrids. Figure 2d shows the high-resolution XPS spectrum of O 1s peaks. The main peak located at 529.3 eV is assigned to O^{2-} in the hybrid. Notably, an additional broad peak at 531.6 eV appears in the spectrum, which is attributed to the oxygen species chemisorbed at oxygen vacancies. This reveals that the oxygen vacancies are stabilized by the adsorbed oxygen species, demonstrating the abundant oxygen defects in WO$_3$ nanobricks.

The morphology of the WO$_3$-Au semiconductor/metal hybrids was tuned by adding different amounts of chloroauric acid in the synthesis process. Figure 3a,b shows the SEM images of WO$_3$-Au with 1.4 and 2.1 wt % Au, respectively. Noticeably, larger surface areas of the WO$_3$ nanobrick are covered with Au nanoparticles. The distance between the Au particles is obviously shortened as the content of Au is increased. The optical properties of WO$_3$-Au hybrids were further investigated. Figure 3c shows the Raman spectra of WO$_3$ nanobricks and WO$_3$-Au with different contents of Au. The characteristic peaks located at 275 and 328 cm^{-1} are ascribed to the bending vibration mode of O−W−O. The peaks at 712 and 810 cm^{-1} originate from the stretching vibration mode of W−O. Noticeably, both types of modes are improved in the presence of Au, owing to the plasmon-induced electromagnetic enhancement. The intensities of these two modes are further amplified by increasing the amount of Au. This may be caused by more electromagnetic hotspots being generated by strong plasmon coupling from the surface-deposited Au nanoparticles. Figure 3d shows the extinction spectra of WO$_3$ and WO$_3$-Au hybrids with different contents of Au. Pure WO$_3$ nanobricks only have an extinction band covering the visible light region, which may be caused by the adjustment of the band gap in the presence of oxygen vacancies. In the presence of Au, an arresting plasmon resonance band at around 580 nm was found in the extinction spectrum of WO$_3$-Au (0.7 wt %), demonstrating the improved visible light-harvesting ability compared with pure WO$_3$. The plasmon peak red-shifts and broadens as the content of Au increases, revealing the prominent visible light-harvesting ability, laying the foundation for excellent SERS and photocatalytic applications.

The SERS behaviors of these materials are tested using RhB as a target molecule under the excitation of a 532 nm laser. Figure 4a shows the Raman spectra of RhB with different concentrations absorbed on WO$_3$ nanobricks. The Raman peak located at 613 cm^{-1} is attributed to the C−C−C ring in-plane vibration movement of the RhB molecule. The peaks located at 1360, 1512, and 1647 cm^{-1} are ascribable to C−C stretching modes. Decreasing the concentration of RhB is highly conducive for Raman signal recognition, and the main characteristic peaks (1647 cm^{-1}) in each spectrum can be clearly identified. Even when the concentration of the RhB solution is decreased to 10^{-8} M, the SERS signal is still detectable, indicating the good detection limit of the WO$_3$ nanobricks. To quantize the SERS performance, the enhancement factor (EF) is calculated using the formula

$$ \mathrm{EF} = \frac{I_{\mathrm{SERS}}/N_{\mathrm{SERS}}}{I_{\mathrm{RS}}/N_{\mathrm{RS}}} $$

where I_{SERS} and I_{RS} represent the intensity of SERS and normal Raman signals, respectively. N_{SERS} and N_{RS} refer to the average number of molecules within the laser spot excited by SERS and normal Raman spectroscopy, respectively. The value of $N_{\mathrm{RS}}/N_{\mathrm{SERS}}$ was estimated with the ratio of the respective molecule concentrations according to previous studies.[41,42] At the concentration of 10^{-8} M, the EF reaches 2.0×10^6 for the WO$_3$ nanobricks calculated with the intensity of 1647 cm^{-1}, compared with the normal Raman spectrum of pure RhB tested on a glass slide. The excellent SERS performance may be because of the charge transfer between RhB and the WO$_3$ nanobricks. Meanwhile, the abundant oxygen vacancies of

WO$_3$, demonstrated by XPS analysis, can play an important role in improving surface activity and promoting the charge transfer,[43−45] thereby further improving the SERS activity. Especially, the surface oxygen vacancies on WO$_3$ can offer more active sites for the adsorption of RhB, thereby increasing the affinity for the adsorbent−adsorbate interaction, which further increases the SERS signals via the charge-transfer mechanism. In addition, the energy level of oxygen vacancies in the band gap of WO$_3$ may adjust the energy match and optimize the photoinduced charge-transfer process between the semiconductor and RhB, thus improving the SERS performance.

We further investigated the SERS performance of WO$_3$-Au semiconductor/metal nanobricks. Figure 4b shows the Raman spectra of RhB (10^{-6} M) absorbed on Au nanoparticles and WO$_3$-Au with different contents of Au, revealing that the WO$_3$-Au hybrids show a much higher SERS signal than bare WO$_3$ nanobricks. Particularly, the Raman intensity at 1647 cm^{-1} of the WO$_3$-Au (0.7%) hybrids is 1.98 and 5.86 times that of Au nanoparticles and WO$_3$ (see Figure 4c), respectively. The enhancement mechanism is attributed to the synergistic effect of electromagnetic enhancement and charge transfer between Au and WO$_3$. Most interestingly, the SERS signal of the WO$_3$-Au hybrids is very sensitive to the content of Au, which is greatly enhanced as the content of Au increases to 2.1 wt % (see Figure 4b). The Raman intensity at 1647 cm^{-1} of WO$_3$-Au (2.1 wt %) is 10.4 and 3.51 times that of pure WO$_3$ and Au nanoparticles, respectively (see Figure 4c). To evaluate the reproducibility, 15 different points on the as-prepared WO$_3$-Au (2.1 wt %) were chosen for SERS measurements. Figure S4a shows the Raman spectra collected at 15 random points, which indicate the good stability of the SERS signals. The relative standard deviation (RSD) at 1647 cm^{-1} is about 5.6% (see Figure S4b), indicating excellent uniformity and high reproducibility of the as-prepared substrates. To evaluate the detection sensitivity of the WO$_3$-Au hybrids, RhB solutions with different concentrations ranging from 10^{-6} to 10^{-12} M were used as the probe molecules. Figure 4d shows that the WO$_3$-Au hybrids have excellent sensitivity in a wide concentration range. The lowest detectable limit reaches 10^{-12} M, and the maximum EF is calculated to be 5.3×10^8 (at 1647 cm^{-1}). The variation curve based on the concentration of RhB and the Raman intensity at 1647 cm^{-1} is shown in Figure 4e. The logarithmic curve shows good linearity as the concentration changes from 10^{-6} to 10^{-12} M (the inset), indicating the high sensitivity and the wide quantitation range of the WO$_3$-Au (2.1 wt %) hybrids. To further understand the physical mechanism behind the excellent SERS performance, the interfacial electric field of the WO$_3$ and WO$_3$-Au hybrids were calculated. Figure 4f shows the calculated electric field distributions of the WO$_3$ and WO$_3$-Au hybrids with different amounts of Au nanoparticles excited at 532 nm. Compared with the bare WO$_3$ nanobrick, the electric field around the interface between Au and the WO$_3$ substrate shows an obvious enhancement. This interfacial electromagnetic enhancement can not only amplify the SERS signals but also accelerate the charge transfer between Au and WO$_3$, further enhancing the SERS sensitivity. The interfacial hotspots can be further increased by adding more Au nanoparticles. Moreover, a strong enhancement of the electromagnetic field around the interface of two adjacent Au nanoparticles is observed, resulting from the plasmon coupling of Au nanoparticles. This reveals that the high SERS activity of
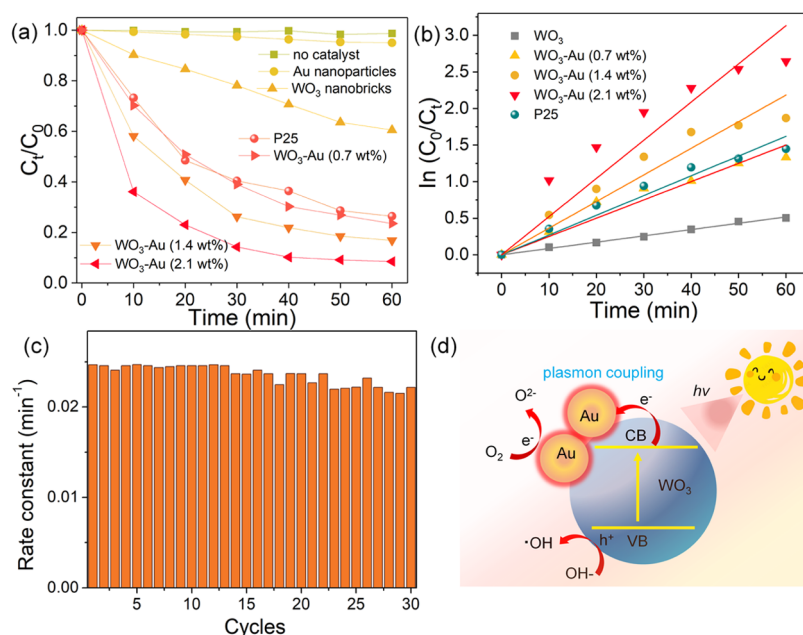
Figure 5. Photocatalytic activities of WO_3 and WO_3-Au hybrids. (a) Photodegradation curves of RhB in the presence of WO_3, commercial P25, and WO_3-Au hybrids with different amounts of Au. (b) Logarithm of the absorption at 550 nm vs reduction time irradiated at visible light. (c) Photocatalytic cycling stability of WO_3-Au (2.1 wt %) hybrids. (d) Proposed photocatalytic mechanism of WO_3-Au hybrids.

the WO_3-Au hybrids with a large content of Au is caused by the more interfacial hotspots between Au and WO_3 and the strong plasmon coupling-induced electric field enhancement. The more the Au nanoparticles deposited on WO_3 nanobricks, the more and stronger the plasmon coupling-induced electromagnetic hotspots, thus endowing WO_3-Au (2.1 wt %) with excellent SERS sensibility. In addition, on further increasing the mass ratio of Au to 2.9 wt %, the SERS signals are decreased compared with WO_3-Au (2.1 wt %) (see Figure S5). This may be caused by the excessive aggregation of Au, which may weaken the plasmonic coupling.[43]

We thereby applied the WO_3 and WO_3-Au hybrids to photocatalytic degradation of the RhB dye under visible light irradiation. The photocatalytic activities were evaluated by monitoring the absorption intensity of the characteristic peak (552 nm) of RhB. Figure 5a shows the degradation curves in the presence of WO_3, Au, commercial P25, and WO_3-Au with different contents of Au. It can be seen that about 39.5% of the dyes were degraded by pure WO_3 nanobricks, owing to the weak visible light absorption and the fast recombination rate of the photogenerated carriers. For WO_3-Au (0.7 wt %) hybrids, about 75.6% of the dyes were reduced under the same conditions, and the photocatalytic rate reached 0.025 min^{-1} (see Figure 5b), which is 2.9 times that of pure WO_3 nanobricks. Noticeably, the photocatalytic activity of WO_3-Au hybrids is further improved by increasing the content of Au. WO_3-Au (2.1 wt %) has the fastest photocatalytic rate, reaching 0.053 min^{-1}, which is 2.1, 6.1, and 2.0 times that of WO_3-Au (0.7 wt %), pure WO_3 nanobricks, and P25, respectively, indicating its potential commercial application. Figure 5c displays the photocatalytic stability test of the WO_3-Au (2.1 wt %) hybrids. The photocatalytic rate remains at about 90% after 30 h of the reaction, indicating good photocatalytic stability. The SEM image of the WO_3-Au hybrids obtained after 30 h of the reaction is shown in Figure S6; the morphology changes little, demonstrating the prominent resistance to photocorrosion. To show the physical

mechanism of the enhanced photocatalytic activity, the band structure and the possible catalytic reaction of the WO_3-Au hybrids are proposed in Figure 5d. Under visible light irradiation, the plasmon resonance of Au nanoparticles can be excited, which can improve the light-harvesting ability of the WO_3-Au hybrids. Meanwhile, the strong electric field of Au can enhance the band gap absorption and charge generation of WO_3. Moreover, the charge transfer between Au and WO_3 can speed up the carrier separation, thereby enhancing the photocatalytic performance. Upon light irradiation, electrons in the valence band (VB) of WO_3 are excited to the conduction band (CB), and the same number of holes are generated in the VB. Driven by potential energy, the photogenerated electrons in the CB of WO_3 can be transferred to Au, which has been reported in previous studies.[46,47] In the photocatalytic processes, the electrons on Au can directly react with the adsorbed O_2 on the surface of samples to produce O^{2-}.[29] Additionally, the photogenerated electrons on WO_3 are transferred to Au to offer more electrons for the reduction reaction. Meanwhile, the holes generated on WO_3 directly react with OH^- to produce hydroxyl radicals,[29] and then efficiently degrade RhB molecules. For the WO_3-Au (2.1 wt %) hybrids, the strong plasmon coupling between Au nanoparticles occurs due to their shortened distance, which can result in wide spectral light absorption, strong electric field, and abundant hot electrons, thereby largely improving the photocatalytic activity. Additionally, it is found that the photocatalytic activity of WO_3-Au (2.9 wt %) is decreased compared with WO_3-Au (2.1 wt %) (see Figure S5). The excess Au nanoparticles on WO_3 may act as recombination centers, which can lower the rate of charge separation, thereby weakening the photocatalytic performance.[29]

3. CONCLUSIONS

In summary, WO_3 nanobricks and WO_3-Au hybrids were prepared through a facile hydrothermal method, which show excellent SERS sensitivity and photocatalytic activity toward

detection and degradation of RhB. The pure WO_3 nanobricks have a SERS enhancement factor of 2.0×10^6 and a limit of detection of 10^{-8} M under a 532 nm laser extrication, due to the charger-transfer property and abundant oxygen vacancies. Owing to the synergistic effect of electromagnetic enhancement and charge transfer, WO_3-Au hybrids display much higher SERS signals than the Au and WO_3 components. The SERS enhancement can be further promoted by increasing the content of Au from 0.7 to 2.1 wt %. The maximum EF of WO_3-Au (2.1 wt %) reaches 5.3×10^8 and the limit of detection is lowered to 10^{-12} M, caused by the strong plasmon coupling-induced electromagnetic field enhancement. Additionally, equipped with strong visible light absorption and electromagnetic fields, the WO_3-Au hybrids also exhibit excellent photocatalytic activity toward degradation of RhB under visible light irradiation. WO_3-Au (2.1 wt %) possesses the fastest photocatalytic rate, which is 6.1 and 2.0 times that of pure WO_3 nanobricks and commercial P25, respectively. Our findings offer potential strategies for enhancing the SERS and photocatalytic performances, and the materials we prepared may be used in the fields of solar cells and water evaporation.

4. EXPERIMENT SECTION

4.1. Reagent. Sodium tungstate (99.5%), chloroauric acid (99.9%), L-ascorbic acid (99.7%), and hydrochloric acid (30%) were purchased from Sinopharm Chemical Reagent Co. Ltd. (Shanghai, China). Deionized water with a resistivity of about 18.25 $M\Omega \cdot cm$ was used as the solvent in all experiments.

4.2. Synthesis of WO_3 and Au-Decorated WO_3 Nanobricks. The WO_3 nanobricks were synthesized by a simple hydrothermal method. Typically, 20 mL of sodium tungstate (0.01 M) and 6 mL of chloroauric acid were added to a reactor. The mixture solution was transferred to an oven and kept at 180 °C for 24 h. The final products were centrifuged at 5000 rpm for 5 min to remove impurities. To synthesize Au-decorated WO_3 nanobricks, 0.01 mg of WO_3 nanobricks and 2 mL of sodium iodide (0.05 M) were added to a 50 mL test tube. Then, 0.5 mL of chloroauric acid (10 mM) and 0.5 mL of L-ascorbic acid (0.1 M) were added. The mixture solution was transferred to an oven and kept at 70 °C for 4 h. The final products were centrifuged and dried at 60 °C to obtain WO_3-Au powders.

4.3. SERS Measurements. RhB molecules were deposited on WO_3 and WO_3-Au hybrids as substrates. The substrates were prepared by adding 1 mL of RhB of a given concentration to 0.5 mL of WO_3 and WO_3-Au (0.5 mg mL^{-1}). The mixture solution was stirred and kept in the dark for 2 h to ensure adequate absorption of RhB. Finally, 0.02 mL of the suspension was dropped onto a clean glass slide and dried at 70 °C for 2 h. Raman spectra were obtained on a Raman spectrometer under excitation at 532 nm (1 mW) for 10 s of acquisition time. Raman spectra from three different positions were obtained for each sample.

4.4. Photocatalytic Measurements. The photocatalytic performances of WO_3 and WO_3-Au hybrids were tested by the photodegradation of RhB under irradiation of a 300 W xenon lamp equipped with an ultraviolet cutoff filter ($\lambda > 420$ nm). Briefly, 10 mL of photocatalysts (0.2 mg mL^{-1}) was added to 20 mL of RhB (10^{-5} M). The mixture solution was stirred continuously during irradiation, and samples were taken every 10 min for further tests. The concentration of RhB was calculated by measuring the extinction density at 552 nm.

4.5. Numerical Simulation. Commercial software (COM-SOL Multiphysics) was used for the finite-element method (FEM) simulations. The refractive index of water is 1.33, and refractive indices of Au and WO_3 were taken from refs 48, 49. Perfectly matched layers were used in the simulations. The detailed structures of WO_3 and WO_3-Au hybrids are taken from the SEM and TEM images.

4.6. Sample Characterization. The TEM images were obtained using a JEOL 2100 operated at 200 kV. HRTEM and EDS were performed using a JEOL 2010 FET microscope operated at a 200 kV accelerating voltage. SEM images were obtained using a FEG SEM Sirion 200 operated at an accelerating voltage of 25.0 kV. XPS spectra were measured using a Thermo Scientific ESCALAB 250Xi system. The extinction spectra were obtained using UV−vis−NIR spectrophotometry (TU1810, Beijing Pgeneral).

■ ASSOCIATED CONTENT

Ⓢ Supporting Information

The Supporting Information is available free of charge at https://pubs.acs.org/doi/10.1021/acsomega.1c04536.

> Low-magnification SEM image of WO_3 nanobricks; EDS spectrum of Au-decorated WO_3 hybrids; XPS survey of WO_3-Au hybrids; measurements of SERS spectral reproducibility; SEM image, SERS, and photocatalytic performances of WO_3-Au (2.1 wt %) hybrids; and SEM image of WO_3-Au (2.1 wt %) after 30 h of photocatalytic reaction (PDF)

■ AUTHOR INFORMATION

Corresponding Authors

Liang Ma − *Hubei Key Laboratory of Optical Information and Pattern Recognition, Wuhan Institute of Technology, Wuhan 430205, P. R. China;* ⓞ orcid.org/0000-0002-9636-118X; Email: maliang@wit.edu.cn

Hua-Yi Hou − *Hubei Key Laboratory of Optical Information and Pattern Recognition, Wuhan Institute of Technology, Wuhan 430205, P. R. China;* Email: hhy@wit.edu.cn

Si-Jing Ding − *School of Mathematics and Physics, China University of Geosciences (Wuhan), Wuhan 430074, P. R. China;* Email: dingsijing@cug.edu.cn

Authors

Jing-Wen Zou − *Hubei Key Laboratory of Optical Information and Pattern Recognition, Wuhan Institute of Technology, Wuhan 430205, P. R. China*

Zhi-Di Li − *Hubei Key Laboratory of Optical Information and Pattern Recognition, Wuhan Institute of Technology, Wuhan 430205, P. R. China*

Hao-Sen Kang − *Hubei Key Laboratory of Optical Information and Pattern Recognition, Wuhan Institute of Technology, Wuhan 430205, P. R. China*

Wen-Qin Zhao − *Hubei Key Laboratory of Optical Information and Pattern Recognition, Wuhan Institute of Technology, Wuhan 430205, P. R. China*

Jing-Chuang Liu − *Hubei Key Laboratory of Optical Information and Pattern Recognition, Wuhan Institute of Technology, Wuhan 430205, P. R. China*

You-Long Chen − *Hubei Key Laboratory of Optical Information and Pattern Recognition, Wuhan Institute of Technology, Wuhan 430205, P. R. China*

Complete contact information is available at:

Author Contributions

§J.-W.Z., Z.-D.L., and H.-S.K. contributed equally to this work.

Notes

The authors declare no competing financial interest.

■ REFERENCES

(1) Demirel, G.; Usta, H.; Yilmaz, M.; Celik, M.; Alidagi, H. A.; Buyukserin, F. Surface-Enhanced Raman Spectroscopy (SERS): an Adventure from Plasmonic Metals to Organic Semiconductors as SERS Platforms. *J. Mater. Chem. C* 2018, 6, 5314−5335.

(2) Park, J. E.; Yonet-Tanyeri, N.; Vander Ende, E.; Henry, A. I.; Perez White, B. E.; Mrksich, M.; Van Duyne, R. P. Plasmonic Microneedle Arrays for in Situ Sensing with Surface-Enhanced Raman Spectroscopy (SERS). *Nano Lett.* 2019, 19, 6862−6868.

(3) Lee, K. L.; Hung, C. Y.; Pan, M. Y.; Wu, T. Y.; Yang, S. Y.; Wei, P. K. Dual Sensing Arrays for Surface Plasmon Resonance (SPR) and Surface-Enhanced Raman Scattering (SERS) Based on Nanowire/Nanorod Hybrid Nanostructures. *Adv. Mater. Interfaces* 2018, 5, No. 1801064.

(4) Kisch, H. Semiconductor Photocatalysis-Mechanistic and Synthetic Aspects. *Angew. Chem., Int. Ed.* 2013, 52, 812−847.

(5) Zhou, C.; Lai, C.; Zhang, C.; Zeng, G.; Huang, D.; Cheng, M.; Jiang, L.; et al. Semiconductor/Boron Nitride Composites: Synthesis, Properties, and Photocatalysis Applications. *Appl. Catal., B* 2018, 238, 6−18.

(6) Xu, K.; Zhou, R.; Takei, K.; Hong, M. Toward Flexible Surface-Enhanced Raman Scattering (SERS) Sensors for Point-of-Care Diagnostics. *Adv. Sci.* 2019, 6, No. 1900925.

(7) Tong, L.; Xu, H.; Käll, M. Nanogaps for SERS Applications. *MRS Bull.* 2014, 39, 163−168.

(8) Park, W. H.; Kim, Z. H. Charge Transfer Enhancement in the SERS of a Single Molecule. *Nano Lett.* 2010, 10, 4040−4048.

(9) Ji, W.; Li, L.; Song, W.; Wang, X.; Zhao, B.; Ozaki, Y. Enhanced Raman Scattering by ZnO Superstructures: Synergistic Effect of Charge Transfer and Mie Resonances. *Angew. Chem., Int. Ed.* 2019, 58, 14452−14456.

(10) Park, S.; Lee, J.; Ko, H. Transparent and Flexible Surface-Enhanced Raman Scattering (SERS) Sensors Based on Gold Nanostar Arrays Embedded in Silicon Rubber Film. *ACS Appl. Mater. Interfaces* 2017, 9, 44088−44095.

(11) Liu, G.; Li, Y.; Duan, G.; Wang, J.; Liang, C.; Cai, W. Tunable Surface Plasmon Resonance and Strong SERS Performances of Au Opening-Nanoshell Ordered Arrays. *ACS Appl. Mater. Interfaces* 2012, 4, 1−5.

(12) Cardinal, M. F.; Vander Ende, E.; Hackler, R. A.; McAnally, M. O.; Stair, P. C.; Schatz, G. C.; Van Duyne, R. P. Expanding Applications of SERS through Versatile Nanomaterials Engineering. *Chem. Soc. Rev.* 2017, 46, 3886−3903.

(13) He, L.; Liu, C.; Tang, J.; Zhou, Y.; Yang, H.; Liu, R.; Hu, J. Self-Catalytic Stabilized Ag-Cu Nanoparticles with Tailored SERS Response for Plasmonic Photocatalysis. *Appl. Surf. Sci.* 2018, 434, 265−272.

(14) Wang, K.; Sun, D. W.; Pu, H.; Wei, Q.; Huang, L. Stable, Flexible, and High-Performance SERS Chip Enabled by a Ternary Film-Packaged Plasmonic Nanoparticle Array. *ACS Appl. Mater. Interfaces* 2019, 11, 29177−29186.

(15) Ma, L.; Chen, Y. L.; Song, X. P.; Yang, D. J.; Li, H. X.; Ding, S. J.; Chen, X. B.; et al. Structure-Adjustable Gold Nanoingots with Strong Plasmon Coupling and Magnetic Resonance for Improved Photocatalytic Activity and SERS. *ACS Appl. Mater. Interfaces* 2020, 12, 38554−38562.

(16) Cong, S.; Yuan, Y.; Chen, Z.; Hou, J.; Yang, M.; Su, Y.; Zhao, Z.; et al. Noble Metal-Comparable SERS Enhancement from Semiconducting Metal Oxides by Making Oxygen Vacancies. *Nat. Commun.* 2015, 6, No. 7800.

(17) Wu, H.; Wang, H.; Li, G. Metal Oxide Semiconductor SERS-Active Substrates by Defect Engineering. *Analyst* 2017, 142, 326−335.

(18) Musumeci, A.; Gosztola, D.; Schiller, T.; Dimitrijevic, N. M.; Mujica, V.; Martin, D.; Rajh, T. SERS of Semiconducting Nanoparticles (TiO_2 Hybrid Composites). *J. Am. Chem. Soc.* 2009, 131, 6040−6041.

(19) Song, G.; Gong, W.; Cong, S.; Zhao, Z. Ultrathin Two-Dimensional Nanostructures: Surface Defects for Morphology-Driven Enhanced Semiconductor SERS. *Angew. Chem., Int. Ed.* 2021, 60, 5505−5511.

(20) Li, M.; Fan, X.; Gao, Y.; Qiu, T. $W_{18}O_{49}$/Monolayer MoS_2 Heterojunction-Enhanced Raman Scattering. *J. Phys. Chem. Lett.* 2019, 10, 4038−4044.

(21) Shutov, A. D.; Yi, Z.; Wang, J.; Sinyukov, A. M.; He, Z.; Tang, C.; Scully, M. O.; et al. Giant Chemical Surface Enhancement of Coherent Raman Scattering on MoS_2. *ACS Photonics* 2018, 5, 4960−4968.

(22) Muehlethaler, C.; Considine, C. R.; Menon, V.; Lin, W. C.; Lee, Y. H.; Lombardi, J. R. Ultrahigh Raman Enhancement on Monolayer MoS_2. *ACS Photonics* 2016, 3, 1164−1169.

(23) Zhong, S.; Xi, Y.; Wu, S.; Liu, Q.; Zhao, L.; Bai, S. Hybrid Cocatalysts in Semiconductor-Based Photocatalysis and Photoelectrocatalysis. *J. Mater. Chem. A* 2020, 8, 14863−14894.

(24) Wang, F.; Li, Q.; Xu, D. Recent Progress in Semiconductor-Based Nanocomposite Photocatalysts for Solar-To-Chemical Energy Conversion. *Adv. Energy Mater.* 2017, 7, No. 1700529.

(25) Hoffmann, M. R.; Martin, S. T.; Choi, W.; Bahnemann, D. W. Environmental Applications of Semiconductor Photocatalysis. *Chem. Rev.* 1995, 95, 69−96.

(26) Meng, X.; Liu, L.; Ouyang, S.; Xu, H.; Wang, D.; Zhao, N.; Ye, J. Nanometals for Solar-To-Chemical Energy Conversion: From Semiconductor-Based Photocatalysis to Plasmon-Mediated Photocatalysis and Photo-Thermocatalysis. *Adv. Mater.* 2016, 28, 6781−6803.

(27) Shaik, F.; Peer, I.; Jain, P. K.; Amirav, L. Plasmon-enhanced Multicarrier Photocatalysis. *Nano Lett.* 2018, 18, 4370−4376.

(28) Yu, G.; Qian, J.; Zhang, P.; Zhang, B.; Zhang, W.; Yan, W.; Liu, G. Collective Excitation of Plasmon-Coupled Au-Nanochain Boosts Photocatalytic Hydrogen Evolution of Semiconductor. *Nat. Commun.* 2019, 10, No. 4912.

(29) Han, S.; Hu, L.; Gao, N.; Al-Ghamdi, A. A.; Fang, X. Efficient Self-Assembly Synthesis of Uniform CdS Spherical Nanoparticles-Au Nanoparticles Hybrids with Enhanced Photoactivity. *Adv. Funct. Mater.* 2014, 24, 3725−3733.

(30) Shi, R.; Cao, Y.; Bao, Y.; Zhao, Y.; Waterhouse, G. I. N.; Fang, Z.; Zhang, T.; et al. Self-Assembled Au/CdSe Nanocrystal Clusters for Plasmon-Mediated Photocatalytic Hydrogen Evolution. *Adv. Mater.* 2017, 29, No. 1700803.

(31) Siddhanta, S.; Thakur, V.; Narayana, C.; Shivaprasad, S. M. Universal Metal-Semiconductor Hybrid Nanostructured SERS Substrate for Biosensing. *ACS Appl. Mater. Interfaces* 2012, 4, 5807−5812.

(32) Liu, Y.; Ma, H.; Han, X. X.; Zhao, B. Metal-Semiconductor Heterostructures for Surface-Enhanced Raman Scattering: Synergistic Contribution of Plasmons and Charge Transfer. *Mater. Horiz.* 2021, 8, 370−382.

(33) Yang, T.; Liu, W.; Li, L.; Chen, J.; Hou, X.; Chou, K. C. Synergizing the Multiple Plasmon Resonance Coupling and Quantum Effects to Obtain Enhanced SERS and PEC Performance Simultaneously on A Noble Metal-Semiconductor Substrate. *Nanoscale* 2017, 9, 2376−2384.

(34) Zhou, J.; Zhang, J.; Yang, H.; Wang, Z.; Shi, J. A.; Zhou, W.; He, S.; et al. Plasmon-Induced Hot Electron Transfer in Au-ZnO

Heterogeneous Nanorods for Enhanced SERS. *Nanoscale* **2019**, *11*, 11782−11788.

(35) Liu, L.; Yang, H.; Ren, X.; Tang, J.; Li, Y.; Zhang, X.; Cheng, Z. Au-ZnO Hybrid Nanoparticles Exhibiting Strong Charge-Transfer-Induced SERS for Recyclable SERS-Active Substrates. *Nanoscale* **2015**, *7*, 5147−5151.

(36) Yang, J. L.; Xu, J.; Ren, H.; Sun, L.; Xu, Q. C.; Zhang, H.; Tian, Z. Q.; Li, J. F. In Situ SERS Study of Surface Plasmon Resonance Enhanced Photocatalytic Reactions Using Bifunctional Au@CdS Core-Shell Nanocomposites. *Nanoscale* **2017**, *9*, 6254−6258.

(37) Yang, C.; Qing, C.; Wang, Q.; Zhang, X.; Lou, J.; Liu, Y. Synthesis of the Hybrid CdS/Au Flower-Like Nanomaterials and Their SERS Application. *Sens. Actuators, B* **2020**, *304*, No. 127218.

(38) Han, R.; Song, W.; Wang, X.; Mao, Z.; Han, X. X.; Zhao, B. Investigation of Charge Transfer at the TiO_2-MBA-Au Interface Based on Surface-Enhanced Raman Scattering: SPR Contribution. *Phys. Chem. Chem. Phys.* **2018**, *20*, 5666−5673.

(39) Wang, X.; Zhu, X.; Shi, H.; Chen, Y.; Chen, Z.; Zeng, Y.; Duan, H. Three-dimensional-stacked Gold Nanoparticles with Sub-5 nm Gaps on Vertically Aligned TiO_2 Nanosheets for Surface-Enhanced Raman Scattering Detection Down to 10 fM Scale. *ACS Appl. Mater. Interfaces* **2018**, *10*, 35607−35614.

(40) Wang, X.; Han, X. X.; Ma, H.; Li, P.; Li, X.; Kitahama, Y.; Ozaki, Y.; Zhao, B. Reduced Charge-Transfer Threshold in Dye-Sensitized Solar Cells with an $Au@Ag/N_3/n$-TiO_2 Structure as Revealed by Surface-Enhanced Raman Scattering. *J. Phys. Chem. C* **2018**, *122*, 12748−12760.

(41) Zhao, X.; Liu, C.; Yu, J.; Li, Z.; Liu, L.; Li, C.; Zhang, C.; et al. Hydrophobic Multiscale Cavities for High-Performance and Self-Cleaning Surface-Enhanced Raman Spectroscopy (SERS) sensing. *Nanophotonics* **2020**, *9*, 4761−4773.

(42) Zhao, X.; Li, C.; Li, Z.; Yu, J.; Pan, J.; Si, H.; Man, B.; et al. In-situ Electrospun Aligned and Maize-Like AgNPs/PVA@Ag Nanofibers for Surface-Enhanced Raman Scattering on Arbitrary Surface. *Nanophotonics* **2019**, *8*, 1719−1729.

(43) Zheng, Z.; Cong, S.; Gong, W.; Xuan, J.; Li, G.; Lu, W.; Zhao, Z.; Geng, F. Semiconductor SERS Enhancement Enabled by Oxygen Incorporation. *Nat. Commun.* **2017**, *8*, No. 1993.

(44) Zhang, Q.; Li, X.; Ma, Q.; Zhang, Q.; Bai, H.; Yi, W.; Xi, G.; et al. A Metallic Molybdenum Dioxide with High Stability for Surface Enhanced Raman Spectroscopy. *Nat. Commun.* **2017**, *8*, No. 14903.

(45) Cong, S.; Yuan, Y.; Chen, Z.; Hou, J.; Yang, M.; Su, Y.; Zhao, Z.; et al. Noble Metal-Comparable SERS Enhancement from Semiconducting Metal Oxides by Making Oxygen Vacancies. *Nat. Commun.* **2015**, *6*, No. 7800.

(46) Durán-Álvarez, J. C.; Del Angel, R.; Ramírez-Ortega, D.; Guerrero-Araque, D.; Zanella, R. An Alternative Method for the Synthesis of Functional Au/WO_3 Materials and Their Use in the Photocatalytic Production of Hydrogen. *Catal. Today* **2020**, *341*, 49−58.

(47) Ng, K. H.; Minggu, L. J.; Jaafar, N. A.; Arifin, K.; Kassim, M. B. Enhanced Plasmonic Photoelectrochemical Response of Au Sandwiched WO_3 Photoanodes. *Sol. Energy Mater. Sol. Cells* **2017**, *172*, 361−367.

(48) Johnson, P. B.; Christy, R. W. Optical Constants of the Noble Metals. *Phys. Rev. B* **1972**, *6*, 4370−4379.

(49) Charles, C.; Martin, N.; Devel, M. Optical Properties of Nanostructured WO_3 Thin Films by Glancing Angle Deposition: Comparison Between Experiment and Simulation. *Surf. Coat. Technol.* **2015**, *276*, 136−140.